



OPEN ACCESS

Multiplexed endoscopic imaging of Barrett's neoplasia using targeted fluorescent heptapeptides in a phase 1 proof-of-concept study

Jing Chen ,¹ Yang Jiang,² Tse-Shao Chang,³ Bishnu Joshi,¹ Juan Zhou,¹ Joel H Rubenstein,¹ Erik J Wamsteker,¹ Richard S Kwon,¹ Henry Appelman,⁴ David G Beer,⁵ Danielle K Turgeon,¹ Eric J Seibel,⁶ Thomas D Wang ^{1,3,7}

► Additional material is published online only. To view, please visit the journal online (<http://dx.doi.org/10.1136/gutjnl-2020-322945>).

¹Internal Medicine, University of Michigan, Ann Arbor, Michigan, USA

²Biomedical Engineering, University of Washington, Seattle, WA, USA

³Mechanical Engineering, University of Michigan, Ann Arbor, Michigan, USA

⁴Pathology, University of Michigan, Ann Arbor, Michigan, USA

⁵Thoracic Surgery, University of Michigan, Ann Arbor, Michigan, USA

⁶Mechanical Engineering, University of Washington, Seattle, WA, USA

⁷Biomedical Engineering, University of Michigan, Ann Arbor, MI, USA

Correspondence to

Dr Thomas D Wang, Internal Medicine, University of Michigan, Ann Arbor, MI 48109, USA; thomaswa@umich.edu

Received 28 August 2020
Revised 15 September 2020
Accepted 17 September 2020
Published Online First
7 October 2020



© Author(s) (or their employer(s)) 2021. Re-use permitted under CC BY-NC. No commercial re-use. See rights and permissions. Published by BMJ.

To cite: Chen J, Jiang Y, Chang T-S, et al. *Gut* 2021;**70**:1010–1013.

MESSAGE

Improved methods for early cancer detection arising from Barrett's oesophagus (BE) are still needed. Imaging molecular expression patterns in BE patients can target neoplasia. We demonstrate a multiplexed fluorescence imaging approach to detect premalignant lesions with two fluorescently labeled heptapeptides specific for EGFR and ErbB2. Twenty-two BE patients underwent endoscopic imaging with a multimodal scanning fiber endoscope (mmSFE). In this pilot study, 92% of neoplastic lesions could be imaged by comparison with pathology, with only 11% false positives. This first-in-human study demonstrates feasibility to concurrently detect multiple targets in vivo and potential for early detection of cancers that are molecularly heterogeneous.

INIEDMORE DETAIL Background

Oesophageal adenocarcinoma (EAC) is a deadly disease that has increased dramatically in incidence over the past several decades.^{1,2} Endoscopic screening with white light illumination and random biopsy is limited by sampling error.³ Dysplasia often presents with flat architecture and patchy distribution.⁴ EGFR and ErbB2 are transmembrane tyrosine kinase receptors that stimulate epithelial cell growth, proliferation and differentiation.⁵ Overexpression of these targets reflects a higher risk for cancer progression.^{6–8} Multiplexed imaging methods take advantage of the broad spectrum of light over the visible and near-infrared (NIR) regimen. We aim to demonstrate clinical feasibility to visualise EGFR and ErbB2 expression simultaneously in vivo to detect Barrett's neoplasia.

Methods

Consecutive patients referred for either evaluation or therapy of Barrett's neoplasia were recruited for the study (NCT03589443). An mmSFE was designed to collect multiplexed fluorescence images concurrently. Target/background (T/B) ratios were calculated for each fluorescence image. More details on the methods and the multiplexed imaging technology can be found in the online supplemental file.

Results

The peptide QRHKPRE specific for EGFR was labelled with Cy5 via a GGGSK linker, (figure 1A).⁹

KSPNPRF, specific for ErbB2, was labelled with IRDye800 via a GGGSC linker (figure 1B).¹⁰ These fluorophores were chosen to minimise overlap between absorbance and emission spectra (figure 1C). The characteristics and stability of fluorescently labelled peptides are shown in online supplemental tables S1–S4. The pharmacology/toxicology study shows no acute adverse effects in animals (online supplemental tables S5 and S6). The phase 1 safety study was performed in n=25 human, and no abnormalities were identified in the laboratory results, urinalysis and ECG for either peptide, and no adverse events were found.

The mmSFE was designed to collect multiplexed fluorescence images (figure 1D–H). Contrast agents were administered, and real-time images were collected from n=22 subjects, table 1 (online supplemental videos S1–S23). Representative white light images are shown for squamous (SQ) and non-dysplastic BE (NDBE) (figure 2A,B). Minimal background was seen following peptide administration. Fluorescence images were collected in separate channels, and coregistered reflectance provided anatomic landmarks for image interpretation. A representative set of in vivo images for HGD and EAC is shown (figure 2C,D). Increased fluorescence intensities were seen from regions of HGD and EAC, and were confirmed by pathology. Immunohistochemistry (IHC) was performed to validate expression of EGFR and ErbB2 on excised specimens (online supplemental figure S1).

The T/B ratios using QRH*-Cy5 and KSP*-IRDye800 were measured from individual patients (figure 3A,B). For SQ (n=2) or NDBE (n=3), a mean (±SD) T/B ratio of 1.28±0.07 for QRH*-Cy5 and 1.33±0.15 for KSP*-IRDye800, respectively, was calculated. The T/B for (n=4) LGD was 1.23±0.05 and 1.18±0.10, respectively. For HGD (n=7) and EAC (n=6), a mean (±SD) T/B ratio of 1.61±0.21 and 1.68±0.24, respectively, was found. Leave-one-out cross-validation (LOOCV) was used to classify results (online supplemental table S7). Support vector machine (SVM) and logistic regression (LR) provided the highest classification accuracy of 91%. The imaging results revealed n=12, 1, 8 and 1 true positives, false positives, true negatives and false negatives, respectively, resulting in 92% sensitivity and 89% specificity. The decision

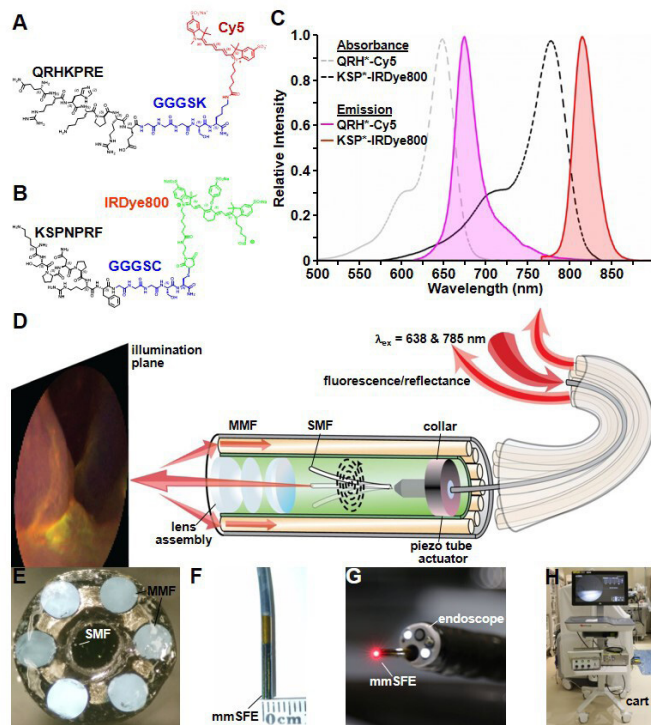


Figure 1 Fluorescently labelled peptides for multiplexed imaging. Biochemical structures are shown for (A) QRH*-Cy5 and (B) KSP*-IRDye800. (C) Peak absorbance of QRH*-Cy5 and KSP*-IRDye800 occurs at $\text{abs}=648$ and 776 nm, respectively. Peak fluorescence emits at $\text{em}=675$ and 812 nm, respectively. (D) Schematic diagram for the multimodal scanning fibre endoscope (mmSFE) is shown. Excitation at $\text{ex}=638$ and 785 nm is delivered through a single-mode fibre (SMF) that is scanned in a spiral pattern by a piezo tube actuator. The beam is focused onto the tissue surface (illumination plane) by a lens assembly. (E) Fluorescence is collected by a ring of large core multi-mode fibres (MMF) mounted around the instrument periphery. (F) The dimensions of the rigid tip are 9 mm in length and 2.4 mm in diameter. (G) This instrument passes forward through the 2.7 mm working channel of a standard medical endoscope (Olympus #GIF-HQ190). (H) The system is contained within a portable cart.

boundaries using SVM and LR are shown. The ROC curves using these methods with LOOCV are displayed (figure 3C). A higher AUC was achieved with multiplexed detection versus either target alone from bootstrap (figure 3D).

Comments

Here, we demonstrate feasibility to detect Barrett's neoplasia endoscopically by imaging two targets concurrently in vivo. Fluorescently labelled peptides specific for epithelial growth factor receptor (EGFR) and epithelial growth factor receptor2 (ErbB2) were administered topically in the distal oesophagus of $n=22$ BE patients. With conventional white light illumination, structural abnormalities associated with Barrett's neoplasia appeared subtle. By comparison, spatial patterns of target expression were visualised with high contrast using fluorescence. Two laser excitation wavelengths were delivered concurrently through a single flexible optical fibre using a prototype-wide-field endoscope accessory. Adequate signal was collected by using large core, high numerical aperture fibres. The regions imaged were compared with histopathology of specimens excised via either endoscopic mucosal

Table 1 Patient demographics

Age	Gender	Prague/stage	Tissue sampling	Pathology
68	M	C0M0I0	EMR/biopsy	SQ
57	M	C0M0I0	biopsy	SQ
84	F	C0M0I9	biopsy	NDBE
60	M	C0M1	EMR/biopsy	NDBE
56	M	C1M3	EMR/biopsy	NDBE
57	M	C7M9	biopsy*	LGD
56	F	C0M1	biopsy*	LGD
80	F	C0M0I0	biopsy*	LGD
67	M	C0M0I7	EMR/biopsy	LGD
79	F	C0M2	biopsy	HGD
88	M	C0M3	EMR/biopsy	HGD
79	M	C0M1I1.5	EMR/biopsy	HGD
85	M	C12M13	biopsy	HGD
79	M	C4M5	biopsy	HGD
66	M	C0M0	biopsy	HGD
60	M	C9M10	biopsy	HGD
75	M	T3N1	biopsy	EAC
73	F	C0M0I2	EMR/biopsy	EAC
81	M	C10M10	biopsy†	EAC
71	M	C9M12I13	EMR/biopsy	EAC
55	F	T1a	biopsy	EAC
64	F	C0M1	EMR/biopsy	EAC

Multiplexed images were collected in vivo from the distal oesophagus of $n=22$ patients with a mean (\pm SD) age of 70.0 ± 10.8 years. SQ, NDBE and LGD were identified in a total of $n=2$, 3 and 4 subjects, respectively. HGD and EAC were found in $n=7$ and 6 subjects, respectively. Modified Prague classification includes length in centimetres of circumferential Barrett's oesophagus (C), maximal tongue (M) and any proximal island (I). These findings were confirmed by histopathology from either EMR or biopsy.

*No tissue sampling performed at time of fluorescence imaging. Pathology based on findings from the most recent pathological reports before and after the imaging procedure.

†A mass was found in the thoracic oesophagus and the tissue diagnosis was obtained prior to this exam.

EAC, oesophageal adenocarcinoma; EMR, endoscopic mucosal resection; HGD, high-grade dysplasia; LGD, low-grade dysplasia; NDBE, non-dysplastic Barrett's oesophagus; SQ, squamous.

resection or biopsy. IHC of these specimens confirmed heterogeneous expression of EGFR and ErbB2.

To our knowledge, this study first demonstrates clinical application of multiplexed fluorescence imaging during endoscopy. Many cancers, including EAC, are molecularly heterogeneous, thus detection of multiple targets is likely to be needed for accurate clinical diagnosis. Mucosal abnormalities with non-specific features, such as nodularity, ulceration and irregularities, may not be relied on to accurately locate Barrett's neoplasia. Several medical societies recommend random 4-quadrant biopsies for EAC surveillance, but this sampling method is inefficient and has been poorly adopted by community physicians.¹¹ Molecular biomarkers can be highly specific for disease, and are expressed well before neoplastic lesions become grossly apparent. Endoscopic imaging strategies for detecting these targets in vivo can be used to guide and prioritise high risk regions for resection, reduce surveillance frequency, and minimise over diagnosis.

Recently, detection of dysplasia and early EAC in BE patients was demonstrated using an antibody specific for vascular endothelial growth factor A. Bevacizumab was originally developed for cancer therapy, and was repurposed for diagnostic imaging by labelling with IRDye800.¹² Compared with antibodies, peptides are smaller in size, have faster binding kinetics, and

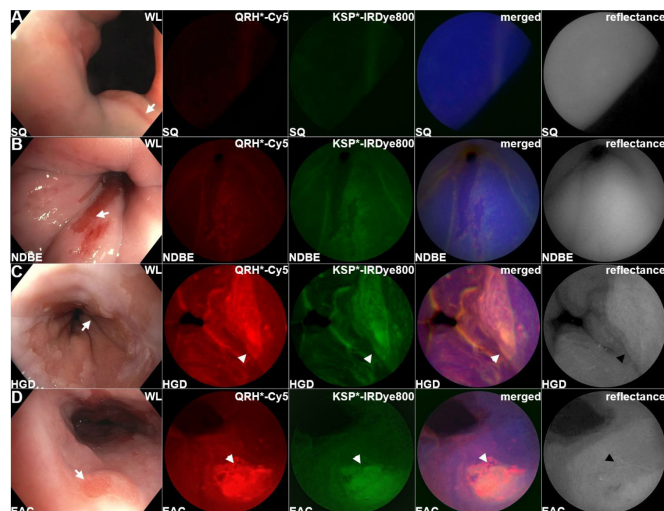


Figure 2 Barrett's oesophagus. Representative in vivo images collected endoscopically are shown from patients with (A) squamous (SQ), (B) non-dysplastic Barrett's oesophagus (NDBE), (C) high-grade dysplasia (HGD) and (D) oesophageal adenocarcinoma (EAC). The presence of NDBE is identified by the salmon red patches (arrows) in the white light images. Fluorescence images are collected after separate topical administration of QRH*-Cy5 and KSP*-IRDye800. The merged images show high contrast regions-of-interest (ROI) where EGFR and ErbB2 (orange) are coexpressed. Coregistered reflectance images provide anatomical landmarks to interpret the location of the ROI's.

can be mass manufactured at lower costs.^{13–15} The peptides were delivered to the mucosal surface in the distal oesophagus using topical administration. This method was effective for staining

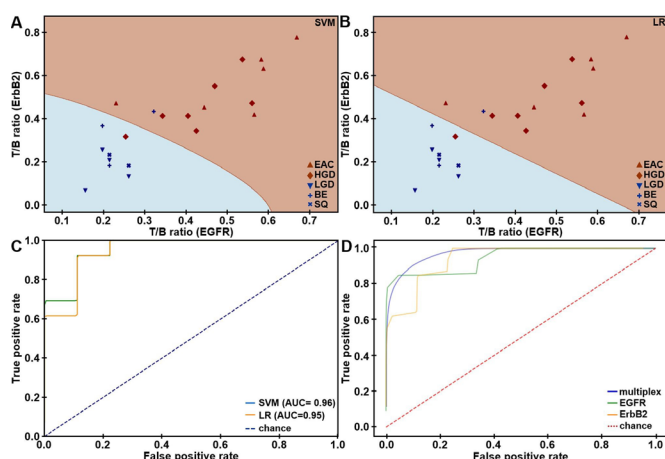


Figure 3 In vivo imaging performance. Scatter plot shows target/background (T/B) ratios measured for EGFR and ErbB2 expression in the fluorescence images collected in vivo from the distal oesophagus of n=22 patients. Decision boundaries show regions classified as either negative (blue) or positive (brown) for neoplasia using (A) support vector machine (SVM) and (B) logistic regression (LR) trained on all data. (C) ROC curves for classifying HGD/EAC from SQ/NDBE/LGD are shown using SVM and LR algorithms with leave-one-out cross-validation (LOOCV). (D) Average ROC curves from bootstrap using SVM (AUC=0.97) model trained on all data show that multiplexed detection provides improved performance than using either EGFR (AUC=0.95) or ErbB2 alone (AUC=0.94). AUC, area under curve; EGFR, epithelial growth factor receptor; ErbB2, epithelial growth factor receptor2; ROC, receiver-operator characteristic.

regions of neoplastic BE involvement.¹⁶ Compared with systemic delivery, this approach localises the distribution of exogenous imaging agents to the target tissues only, minimises background and maximises image contrast. This strategy was chosen because the peptides used have similar binding kinetics.^{9–10} Lectins have been investigated for detection of Barrett's neoplasia ex vivo,¹⁷ but have not been demonstrated clinically. Fluorescently labelled peptides for targeted detection of premalignant lesions in the colon have also been shown clinically.^{18–19} Folate has been developed for targeted imaging of ovarian cancer,²⁰ however, small molecules have limited flexibility for fluorescence labelling and would be difficult to use with multiplexed imaging.

In this work, light over a broad optical spectrum was collected using a flexible fibre endoscope accessory, and was separated into fluorescence and reflectance channels.²¹ Multipixel photon counters with much higher sensitivity than the charge-coupled devices found in video endoscopes were used. Multiplexed detection was achieved by exciting Cy5 and IRDye800 at wavelengths with minimal overlap between the absorption and emission bands. Additional targets can be detected by extending this strategy to the full visible and NIR spectrum.²² Fluorescence emission in the NIR regimen mitigates the effects of haemoglobin absorption and tissue scattering, and minimises tissue autofluorescence background.²³ The distal optics and scan strategy used provide much greater spatial resolution than an optical fibre bundle.

The clinical usefulness of this technology can be improved by addressing several study limitations. The peptides were administered separately to minimise potential binding interactions but can be combined to reduce time needed to reconstitute and prepare the peptides for delivery. After inserting the imaging accessory through the working channel, the fluorescence and HD-WLE images were not oriented. Accurate alignment would allow the fluorescence images to be more effective as a guide for tissue resection. This study was performed at a tertiary referral centre that specialises in treatment of patients with advanced BE, thus a cohort highly enriched with neoplasia was studied. Inclusion of more non-neoplastic subjects would better reflect the prevalence of disease seen in the community. In conclusion, we demonstrated a proof-of-concept study for detecting multiple targets concurrently in patients with Barrett's neoplasia and this strategy is promising for early detection of cancers in other hollow organs.

Acknowledgements We thank E Brady, D Chandrasekhar, and A Cawthon for clinical support, and BR Reisdorph for regulatory support.

Contributors JC, BJ, JZ, DGB, DKT, EJS and TDW conceived and designed the experiments. JC, T-SC, JHR, EJW and RSK performed the experiments. JHR, YJ and EJS contributed to image and data analysis. HA reviewed pathology. JC, YJ, EJS and TDW wrote the manuscript.

Funding This study was supported in part by the National Institutes of Health U54 CA163059 (DGB, JHR, EJS, TDW), U01 CA189291 (TDW) and R01 CA200007 (EJS, TDW).

Competing interests None declared.

Patient consent for publication Not required.

Provenance and peer review Not commissioned; externally peer reviewed.

Supplemental material This content has been supplied by the author(s). It has not been vetted by BMJ Publishing Group Limited (BMJ) and may not have been peer-reviewed. Any opinions or recommendations discussed are solely those of the author(s) and are not endorsed by BMJ. BMJ disclaims all liability and responsibility arising from any reliance placed on the content. Where the content includes any translated material, BMJ does not warrant the accuracy and reliability of the translations (including but not limited to local regulations, clinical guidelines, terminology, drug names and drug dosages), and is not responsible for any error and/or omissions arising from translation and adaptation or otherwise.

Open access This is an open access article distributed in accordance with the Creative Commons Attribution Non Commercial (CC BY-NC 4.0) license, which permits others to distribute, remix, adapt, build upon this work non-commercially, and license their derivative works on different terms, provided the original work is properly cited, appropriate credit is given, any changes made indicated, and the use is non-commercial. See: <http://creativecommons.org/licenses/by-nc/4.0/>.

ORCID iDs

Jing Chen <http://orcid.org/0000-0001-8863-2843>

Thomas D Wang <http://orcid.org/0000-0001-9182-9620>

REFERENCES

- 1 Thrift AP, Whiteman DC. The incidence of esophageal adenocarcinoma continues to rise: analysis of period and birth cohort effects on recent trends. *Ann Oncol* 2012;23:3155–62.
- 2 Siegel RL, Miller KD, Jemal A. Cancer statistics, 2016. *CA Cancer J Clin* 2016;66:7–30.
- 3 Sharma P, Savides TJ, Canto MI, et al. The American Society for gastrointestinal endoscopy PIVI (preservation and incorporation of valuable endoscopic innovations) on imaging in Barrett's esophagus. *Gastrointest Endosc* 2012;76:252–4.
- 4 Spechler SJ, Sharma P, Souza RF, et al. American gastroenterological association technical review on the management of Barrett's esophagus. *Gastroenterology* 2011;140:e18–52.
- 5 Citri A, Yarden Y. EGF-ERBB signalling: towards the systems level. *Nat Rev Mol Cell Biol* 2006;7:505–16.
- 6 Dulak AM, Schumacher SE, van Lieshout J, et al. Gastrointestinal adenocarcinomas of the esophagus, stomach, and colon exhibit distinct patterns of genome instability and oncogenesis. *Cancer Res* 2012;72:4383–93.
- 7 Dulak AM, Stojanov P, Peng S, et al. Exome and whole-genome sequencing of esophageal adenocarcinoma identifies recurrent driver events and mutational complexity. *Nat Genet* 2013;45:478–86.
- 8 Miller CT, Moy JR, Lin L, et al. Gene amplification in esophageal adenocarcinomas and Barrett's with high-grade dysplasia. *Clin Cancer Res* 2003;9:4819–25.
- 9 Zhou J, Joshi BP, Duan X, et al. EGFR overexpressed in colonic neoplasia can be detected on wide-field endoscopic imaging. *Clin Transl Gastroenterol* 2015;6:e101.
- 10 Joshi BP, Zhou J, Pant A, et al. Design and synthesis of near-infrared peptide for in vivo molecular imaging of HER2. *Bioconjug Chem* 2016;27:481–94.
- 11 Kariv R, Plesec TP, Goldblum JR, et al. The Seattle protocol does not more reliably predict the detection of cancer at the time of esophagectomy than a less intensive surveillance protocol. *Clin Gastroenterol Hepatol* 2009;7:653–8.
- 12 Nagengast WB, Hartmans E, Garcia-Allende PB, et al. Near-infrared fluorescence molecular endoscopy detects dysplastic oesophageal lesions using topical and systemic tracer of vascular endothelial growth factor A. *Gut* 2019;68:7–10.
- 13 Lee S, Xie J, Chen X. Peptides and peptide hormones for molecular imaging and disease diagnosis. *Chem Rev* 2010;110:3087–111.
- 14 Wu AM, Senter PD. Arming antibodies: prospects and challenges for immunoconjugates. *Nat Biotechnol* 2005;23:1137–46.
- 15 Conner KP, Rock BM, Kwon GK, et al. Evaluation of near infrared fluorescent labeling of monoclonal antibodies as a tool for tissue distribution. *Drug Metab Dispos* 2014;42:1906–13.
- 16 Sturm MB, Joshi BP, Lu S, et al. Targeted imaging of esophageal neoplasia with a fluorescently labeled peptide: first-in-human results. *Sci Transl Med* 2013;5:184ra161.
- 17 Bird-Lieberman EL, Neves AA, Lao-Sirieix P, et al. Molecular imaging using fluorescent lectins permits rapid endoscopic identification of dysplasia in Barrett's esophagus. *Nat Med* 2012;18:315–21.
- 18 Burggraaf J, Kamerling IMC, Gordon PB, et al. Detection of colorectal polyps in humans using an intravenously administered fluorescent peptide targeted against c-Met. *Nat Med* 2015;21:955–61.
- 19 Joshi BP, Dai Z, Gao Z, et al. Wide-field endoscopic imaging of sessile serrated adenomas with fluorescently-labeled peptide probe. *Gastroenterology* 2017;152:1002–13.
- 20 van Dam GM, Themelis G, Crane LMA, et al. Intraoperative tumor-specific fluorescence imaging in ovarian cancer by folate receptor- α targeting: first in-human results. *Nat Med* 2011;17:1315–9.
- 21 Savastano LE, Zhou Q, Smith A, et al. Multimodal laser-based angioscopy for structural, chemical and biological imaging of atherosclerosis. *Nat Biomed Eng* 2017;1:0023.
- 22 Miller SJ, Lee CM, Joshi BP, et al. Targeted detection of murine colonic dysplasia in vivo with flexible multispectral scanning fiber endoscopy. *J Biomed Opt* 2012;17:021103.
- 23 Ntziachristos V, Bremer C, Weissleder R. Fluorescence imaging with near-infrared light: new technological advances that enable in vivo molecular imaging. *Eur Radiol* 2003;13:195–208.

Multiplexed imaging of Barrett's neoplasia using targeted fluorescent heptapeptides and multimodal scanning fiber endoscope: a phase 1, open-label, proof-of-concept study

Jing Chen,¹ Yang Jiang,² Tse-Shao Chang,³ Bishnu Joshi,¹ Juan Zhou,¹ Joel H Rubenstein,¹ Erik J Wamsteker,¹ Richard S Kwon,¹ Henry Appelman,⁴ David G Beer,⁵ Danielle K Turgeon,¹ Eric J Seibel,² Thomas D Wang^{1,3,7}

Supplementary methods

Fluorescently-labeled peptides

QRHKPRE was labeled with Cy5 via a GGGSK linker to prevent steric hindrance, hereafter QRH*-Cy5. This sequence was selected using phage display methods for specific binding to EGFR. KSPNPRF was labeled with IRDye800 via a GGGSC linker, hereafter KSP*-IRDye800. This sequence was identified using a structural model for specific binding to ErbB2. The fluorophores used were chosen to minimize spectral overlap between absorbance and emission. QRH*-Cy5 and KSP*-IRDye800 were synthesized using current good manufacturing practices (cGMP) methods. Peptide stability was monitored by visual appearance, purity (HPLC), and molecular weight over the duration of the study.

Pharmacology/toxicology study

A rigorous pharmacology/toxicology study was performed in animals (MPI Research) for each peptide to provide pre-clinical evidence for safety. A total of 24 male and 24 female rats (CD[®][CrI:CD[®](SD)] (Charles River) were used in each study. At 8 weeks of age, the animals were randomly assigned to 4 groups, including 3 treatment and 1 control. Dose levels of 0.0086, 0.026, and 0.86 mg/kg were used for QRH*-Cy5, and 0.186, 0.32, and 1.08 mg/kg were used for KSP*-

IRDye800. The control group received 10 mL/kg of PBS as vehicle. The vehicle and test articles were administered by single dose oral gavage. Clinical signs, including morbidity, mortality, and injury, were monitored twice daily. Laboratory tests and necropsy were evaluated in 3 animals/sex/dose on days 2 and 15.

Phase 1 safety study

A first-in-human study was performed to establish clinical evidence of safety for each peptide. An Investigational New Drug (IND) application (sponsor DKT) was prepared, and submitted for review to the US Food and Drug Administration (FDA). The chemistry, manufacturing, and control (CMC) document for cGMP peptide synthesis, animal pharmacology/toxicology results, and study protocol were included. The study protocols were reviewed and approved by the Institutional Review Board (IRB) at Michigan Medicine. These studies, including NCT02574858 (QRH*-Cy5) and NCT03161418 (KSP*-IRDye800), were registered online at ClinicalTrials.gov. A total of n = 25 subjects was recruited for each study. All enrolled patients provided written informed consent. A dose escalation study was performed. The first n = 3 subjects were administered 0.5 mg of peptide reconstituted in 5 mL of normal saline (0.9%) per oral. Laboratory tests, including complete blood count (CBC), chemistries, liver function tests (LFT), and urinalysis (UA), were collected before and ~24 hours after peptide administration. An EKG was performed, and vital signs were monitored. After finding no peptide-related abnormalities, the remaining n = 22 subjects received the higher dose of 1.2 mg. No images were collected during the safety study.

Multiplexed imaging instrument

A multi-modal scanning fiber endoscope (mmSFE) was designed to collect fluorescence and reflectance concurrently. A custom fiber-coupled multi-laser system (SpectraTEC, Blue Sky Research) provides illumination at $\lambda_{\text{ex}} = 638$ and 785 nm concurrently through a single mode fiber (SMF) to excite QRH*-Cy5 and KSP*-IRDye800, respectively. A 0.4 mm diameter metal coated piezo tube actuator (Nagamine) generates a spiral scan pattern at an average maximum deflection angle of $\sim 70^\circ$. Large core (500 μm diameter) multi-mode fibers (MMF) with high numerical aperture (NA = 0.6, Mitsubishi Rayon) are arranged around the instrument periphery to maximize light collection. The diameter and rigid length of the distal tip was compact to pass forward easily through the working channel of a standard upper endoscope.

The optics used to separate and collect fluorescence from each peptide was contained within the base station (VerAvanti). A notch filter (NF, #NF03-785E-25, Semrock) was used to attenuate the excitation beam at $\lambda = 785$ nm. Reflectance at $\lambda = 647$ nm was deflected by a dichroic beam splitter (BS₁, #FF652-Di02, Semrock) to a multi-pixel photon counter (MPPC₁, SiPM, Hamamatsu) for detection. Fluorescence from QRH*-Cy5 was deflected by a second beam splitter (BS₂, #Di02-R785, Semrock) centered at $\lambda = 785$ nm through a bandpass filter (BPF, FF01-697/58, Semrock) that transmits between 668-726 nm for detection by MPPC₂. Fluorescence from KSP*-IRDye800 passes through BS₂ and long pass filter (LPF, #BLP01-785R, Semrock) with cutoff at $\lambda = 805$ nm and is detected by MPPC₃. Kinematic filter cubes (DFM1/M, ThorLabs) were used to mount and align the optics.

In vivo imaging

Consecutive patients referred to Michigan Medicine for either evaluation or therapy of Barrett's neoplasia were recruited. Inclusion criteria included: 1) history of Barrett's neoplasia, 2)

medically able to tolerate upper endoscopy, and 3) age over 18. Exclusion criteria included: 1) history of esophagectomy and 2) on active chemotherapy or radiation protocol. The multiplexed imaging study was approved by the IRB, and was registered online at ClinicalTrials.gov (NCT03589443). All authors had access to the study data, contributed to this manuscript's writing and review, and approved the final manuscript.

The QRH*-Cy5 and KSP*-IRDye800 were reconstituted in 5 mL of normal saline separately, and topically administered in the distal esophagus using a standard spray catheter (PW-5V-1, Olympus Medical Systems Corp) passed through the instrument channel of the endoscope. Separate channels were used to record fluorescence images from QRH*-Cy5 and KSP*-IRDye800 and from reflectance at $\lambda = 638$ nm. The conventional white light illumination was shut off during collection of fluorescence images to prevent interference. Tissue specimens were collected with either biopsy or EMR from suspicious regions. The most advanced histological classification for each subject is shown, Table 1.

Image analysis

Video streams with >30 consecutive fluorescence images (1 sec) having negligible artifacts, including debris, bubbles, pooling, and interference from conventional white light illumination, were extracted from the original recordings. Single frames from the target regions with high contrast and minimum motion blur and distortion were selected for intensity quantification. The frames were separated into two fluorescence channels and a co-registered reflectance image. Target/background (T/B) ratios were calculated for each fluorescence image as follows. A 5×5 Gaussian filter was used first to smooth the image. Fluorescence regions with high intensity were segmented using the Chan-Vese algorithm,¹ where an active contour model was

evolved iteratively to minimize the energy function, Eq. 1, defined by the weighted sum of the 1) boundary length, 2) area, and variance of intensity 3) inside and 4) outside of the segmented region.

$$F(\phi) = \mu \int_{\Omega} |\nabla H(\phi)| dx + \nu \int_{\Omega} H(\phi) dx + \lambda_1 \int_{\Omega} |I - c_1|^2 H(\phi) dx + \lambda_2 \int_{\Omega} |I - c_2|^2 (1 - H(\phi)) dx, \quad (1)$$

where H is the Heaviside function, ϕ is the level set function, I is the segmented image, and Ω is the image domain. Coefficients c_1 and c_2 are the average intensities inside and outside of the segmented region, respectively. The regulation parameters μ , ν , λ_1 , λ_2 represent the energy functions, where μ and ν penalizes the total boundary length and area, respectively, of the segmented region. The intensity variance inside and outside of the segmented regions is represented by λ_1 and λ_2 , respectively.

After image segmentation, a series of standard morphology operations, including erosion and dilation, were implemented using OpenCV library.² Erosion was performed to smooth the target region by removing isolated noise <10 pixels. Dilation was done to enlarge the boundaries of the target region and generate an adjacent 30 pixel-wide background. T/B ratios were calculated from the mean intensities each region. The T/B ratios were used to classify each patient as being either positive (HGD/EAC) or negative (SQ/NDBE/LGD) based on the highest grade of pathology found. Different methods were investigated to classify the data, including the 1,2) T/B ratios from each fluorescence channel separately, 3) maximum T/B ratio, 4) logistic regression with L2 regularization which prevents overfitting of the model, and 5) support vector machine (SVM), which constructs a hyperplane. A leave-one-out cross-validation (LOOCV) was performed to identify the best method.³ For each round, the T/B ratios from $n = 21$ subjects were used as a training set to determine the discriminant function used to assign a score to the left-out subject. For methods 1-3, the maximum Youden index of the receiver operating characteristic (ROC) curve

was used to select the optimal cutoff threshold for HGD/EAC, which maximizes the vertical distance between the ROC curve and the diagonal line.⁴ Normally, the Youden index is defined as sensitivity +, specificity – 1.

For logistic regression and SVM, a nested cross validation was performed to select the hyperparameters for each model, including C-values (inverse of L2 regularization strength) for logistic regression, γ -values (kernel coefficient), and C-values for SVM with a radial basis function (RBF) kernel. A repeated stratified 9-fold cross-validation in the inner loop was used to select the hyperparameters that provided the maximal classification accuracy for the 21 samples. The model was refit with these optimal values using $n = 21$ data points, and then the result left out in the outer loop was evaluated. The average classification accuracy of each method from LOOCV was compared. The sensitivity, specificity, and area-under-the-curve (AUC) for the ROC curve using LOOCV was computed and compared for logistic regression and SVM. The optimal model was then retrained using all data. The performance of multiplexed detection using the trained optimal model was then compared with that for use of either QRH*-Cy5 or KSP*-IRDye800 alone with an average ROC curve taken from 1000 bootstrap samples. The analysis was implemented using Python using scikit-learn library.⁵

Reference

1. Jiang, Y., Gong, Y., Rubenstein, J. H., Wang, T. D. & Seibel, E. J. Toward real-time quantification of fluorescence molecular probes using target/background ratio for guiding biopsy and endoscopic therapy of esophageal neoplasia. *J. Med. Imaging* **4**, 024502 (2017).
2. Bradski, G. & Kaehler, A. in *learning OpenCV* (O'Reilly media, 2008).
3. Kohavi, R. A study of cross-validation and bootstrap for accuracy estimation and model selection. *IJCAI*. **14**, 1137-1145 (1995).
4. Hajian-Tilaki, K. Receiver operating characteristic (ROC) curve analysis for medical diagnostic test evaluation. *Caspian J. Intern. Med.* **4**, 627 (2013).
5. Pedregosa, F. et al. Scikit-learn: machine learning in python, *J. Mach. Learn. Res.* **12**, 2825-2830 (2011).

Supplementary Tables

Supplementary Table 1 – GMP synthesis of QRH*-Cy5

Attributes	Test Methods	Specifications	Results
Appearance	visual	blue powder	blue powder
Purity (%)	HPLC	≥95.0%	96.0%
Amino acid analysis	UPLC	Glx 1.70-2.30	Glx 2.01
		Arg 1.70-2.30	Arg 2.05
		His 0.85-1.15	His 0.98
		Pro 0.85-1.15	Pro 0.99
		Gly 2.55-3.45	Gly 2.97
		Lys 1.70-2.30	Lys 2.01
		Ser report	Ser 0.83
Peptide content	UPLC	report	70.3%
Primary counter ion	HPLC	TFA	TFA
TFA content	HPLC	report	18.5%
Water Content (%w/w)	Karl Fisher	report	5.1%
Endotoxin	SOP	report	<1 EU/mg
Bioburden	SOP	report	<1 CFU/mg
Molecular weight	ESI-MS	1973.3±1.0	1973.0

Note: The final bulk material consisted of Gln¹-Arg²-His³-Lys⁴-Pro⁵-Arg⁶-Glu⁷-Gly⁸-Gly⁹-Gly¹⁰-Ser¹¹-Lys¹²(Cy⁵)-NH₂ with the formula: C₈₆H₁₂₉N₂₆NaO₂₃S₂. Attributes of QRH*-Cy5 are documented on a certificate of analysis (COA) by cGMP vendor. Key: CFU, colony-forming unit; ESI-MS, electrospray ionization mass spectrometry; EU, endotoxin unit; HPLC, high performance liquid chromatography; SOP, standard operating procedure; TFA, trifluoroacetic acid; UPLC, ultra-performance liquid chromatography.

Supplementary Table 2 – GMP synthesis of KSP*-IRDye800

Attributes	Test Methods	Specifications	Results
Appearance	visual	dark green powder	dark green powder
Purity (%)	HPLC	≥95.0%	98.8%
Amino acid analysis	UPLC	Arg 0.85-1.15	Arg 0.99
		Gly 2.55-3.45	Gly 2.96
		Asn 0.85-1.15	Asn 1.05
		Pro 1.70-2.30	Pro 1.99
		Lys 0.85-1.15	Lys 1.00
		Phe 0.85-1.15	Phe 1.02
		Ser report	Ser 1.52
Peptide content	UPLC	Cys report	Cys 0.00
Primary counter ion	HPLC	report	91.9%
Acetic acid content	HPLC	acetate	acetate
Water content (%w/w)	Karl Fisher	report	0.6%
Endotoxin	SOP	report	9.0%
Bioburden	SOP	report	<1 EU/mg
Molecular weight	ESI-MS	report	<1 CFU/mg
		2397.6±1.0	2397.6

Note: The final bulk material consisted of Lys¹-Ser²-Pro³-Asn⁴-Pro⁵-Arg⁶-Phe⁷-Gly⁸-Gly⁹-Gly¹⁰-Ser¹¹-Cys¹²(IRDye800) with the formula: C₁₀₂H₁₃₆N₂₁Na₃O₃₂S₅. Attributes of KSP*-IRDye800 are documented on a certificate of analysis (COA) by cGMP vendor. Key: CFU, colony-forming unit; ESI-MS, electrospray ionization mass spectrometry; EU, endotoxin unit; HPLC, high performance liquid chromatography; SOP, standard operating procedure; UPLC, ultra-performance liquid chromatography.

Supplementary Table 3 – Stability of QRH*-Cy5

Time (Months)	0	6	12	18	24	30	36
Appearance	blue	blue	blue	blue	blue	blue	blue
Purity	96.0%	96.2%	96.3%	97.1%	96.2%	96.4%	96.1%
Molecular Weight	1974.3	N/A	1972.6	N/A	1973.7	N/A	1973.3

Note: Lyophilized peptides are stored at -20°C under dry conditions and are protected from light in an amber tube. Purity was analyzed by high performance liquid chromatography (HPLC). Molecular weight was measured using Q-TOF mass spectrometer.

Supplementary Table 4 – Stability of KSP*-IRDye800

Time (Months)	0	6	12	18	24	30	36
Appearance	dark green	dark green	dark green	dark green	dark green	dark green	dark green
Purity (HPLC)	98.8%	98.8%	98.7%	98.9%	98.9%	98.7%	98.9%
Molecular Weight	2397.6	N/A	2397.5	N/A	2397.6	N/A	2397.6

Note: Lyophilized peptides are stored at -20°C under dry conditions and are protected from light in an amber tube. Purity was analyzed by high performance liquid chromatography (HPLC). Molecular weight was measured using Q-TOF mass spectrometer.

Supplementary Table 5 – Animal pharmacology/toxicology study of QRH*-Cy5

No	Dose level (mg/kg)	Volume (mL/kg)	M	F	Observe	Clinical signs	Blood tests (days 2 and 15)	Necropsy (days 2 and 15)	Urinalysis
1	0	10	6	6	NAD	NAD	NAD	NAD	NAD
2	0.0086	1	6	6	NAD	NAD	NAD	NAD	NAD
3	0.026	1	6	6	NAD	NAD	NAD	NAD	NAD
4	0.86	10	6	6	NAD	NAD	NAD	NAD	NAD

Observe	Clinical signs	Blood tests			Necropsy	Urinalysis
		Hematology	Clinical chemistries	Coagulation factors		
Morbidity, mortality, injury, body weights, food and water consumption	Skin, fur, eyes, ears, nose, oral cavity, thorax, abdomen, external genitalia, limbs and feet; respiratory and circulatory effects; autonomic effects (salivation); nervous system effects (tremors, convulsions, reactivity to handling and unusual behavior)	Leukocyte count (total and absolute differential), erythrocyte count, hemoglobin, hematocrit, mean corpuscular hemoglobin (volume and concentration), platelet count, absolute reticulocytes, blood cell morphology	Alkaline phosphatase, total bilirubin, aspartate aminotransferase, alanine aminotransferase, urea nitrogen, creatinine, total protein, albumin, globulin and A/G (albumin/globulin) ratio, glucose, total cholesterol, triglycerides, sodium, potassium, chloride, calcium, phosphorus	Prothrombin time, activated partial thromboplastin time, fibrinogen	Macroscopic exam for external abnormalities; recording of organ weights; microscopic exam of bone with bone marrow (femur, sternum), brain (cerebrum, midbrain, cerebellum, medulla, pons), esophagus, heart, kidney, liver, lung with bronchi, lymph nodes (mesenteric), small intestine (duodenum, ileum, jejunum), spleen, stomach (glandular, nonglandular) and thymus.	Volume, color and appearance, specific gravity, pH, protein, glucose, bilirubin, ketones, blood, urobilinogen, microscopy of centrifuged sediment

Notes: Acute test article-related effects in 7-week-old CD[CrI:CD(SD)] rats (n = 48) after oral gavage administration of cGMP-synthesized QRH*-Cy5 are shown. Phosphate-buffered saline (pH = 7.4) was used as vehicle. Animal were monitored at specific time points over the course of 15 days after peptide administration. For necropsy, 3 animals/sex/group were euthanized on days 2 and 15. NAD – No abnormalities detected.

Supplementary Table 6 – Animal pharmacology/toxicology study of KSP*-IRDye800

No	Dose level (mg/kg)	Volume (mL/kg)	M	F	Observe	Clinical signs	Blood tests (days 2 and 15)	Necropsy (days 2 and 15)	Urinalysis
1	0	10	6	6	NAD	NAD	NAD	NAD	NAD
2	0.186	10	6	6	NAD	NAD	NAD	NAD	NAD
3	0.32	10	6	6	NAD	NAD	NAD	NAD	NAD
4	1.08	10	6	6	NAD	NAD	NAD	NAD	NAD

Observe	Clinical signs	Blood tests			Necropsy	Urinalysis
		Hematology	Clinical chemistries	Coagulation factors		
Morbidity, mortality, injury, body weights, food and water consumption	Skin, fur, eyes, ears, nose, oral cavity, thorax, abdomen, external genitalia, limbs and feet; respiratory and circulatory effects; autonomic effects (salivation); nervous system effects (tremors, convulsions, reactivity to handling and unusual behavior)	Leukocyte count (total and absolute differential), erythrocyte count, hemoglobin, hematocrit, mean corpuscular hemoglobin (volume and concentration), platelet count, absolute reticulocytes, blood cell morphology	Alkaline phosphatase, total bilirubin, aspartate aminotransferase, alanine aminotransferase, urea nitrogen, creatinine, total protein, albumin, globulin and A/G (albumin/globulin) ratio, glucose, total cholesterol, triglycerides, sodium, potassium, chloride, calcium, phosphorus	Prothrombin time, activated partial thromboplastin time, fibrinogen	Macroscopic exam for external abnormalities; recording of organ weights; microscopic exam of bone with bone marrow (femur, sternum), brain (cerebrum, midbrain, cerebellum, medulla, pons), esophagus, heart, kidney, liver, lung with bronchi, lymph nodes (mesenteric), small intestine (duodenum, ileum, jejunum), spleen, stomach (glandular, nonglandular) and thymus.	Volume, color and appearance, specific gravity, pH, protein, glucose, bilirubin, ketones, blood, urobilinogen, microscopy of centrifuged sediment

Notes: Acute test article-related effects in 7-week-old CD[CrI:CD(SD)] rats (n = 48) after oral gavage administration of cGMP-synthesized KSP*-IRDye800 are shown. Phosphate-buffered saline (pH = 7.4) was used as vehicle. Animal were monitored at specific time points over the course of 15 days after peptide administration. For necropsy, 3 animals/sex/group were euthanized on days 2 and 15. NAD – No abnormalities detected.

Supplementary Table 7 – In vivo imaging results

Methods	Accuracy	AUC
T/B ratio from QRH*-Cy5	86%	0.95
T/B ratio from KSP*-IRDye800	82%	0.94
Maximum T/B ratio	86%	0.96
Support vector machine (SVM)	91%	0.97
Logistic regression	91%	0.97

Notes: Classification accuracy for in vivo images versus highest grade of pathology is shown for different methods using leave-one-out cross-validation (LOOCV). Average AUC with 1000 bootstrap samples using the models trained on all of the data is shown. SVM and logistic regression models combine T/B ratios from QRH*-Cy5 and KSP*-IRDye800.

Supplementary figures

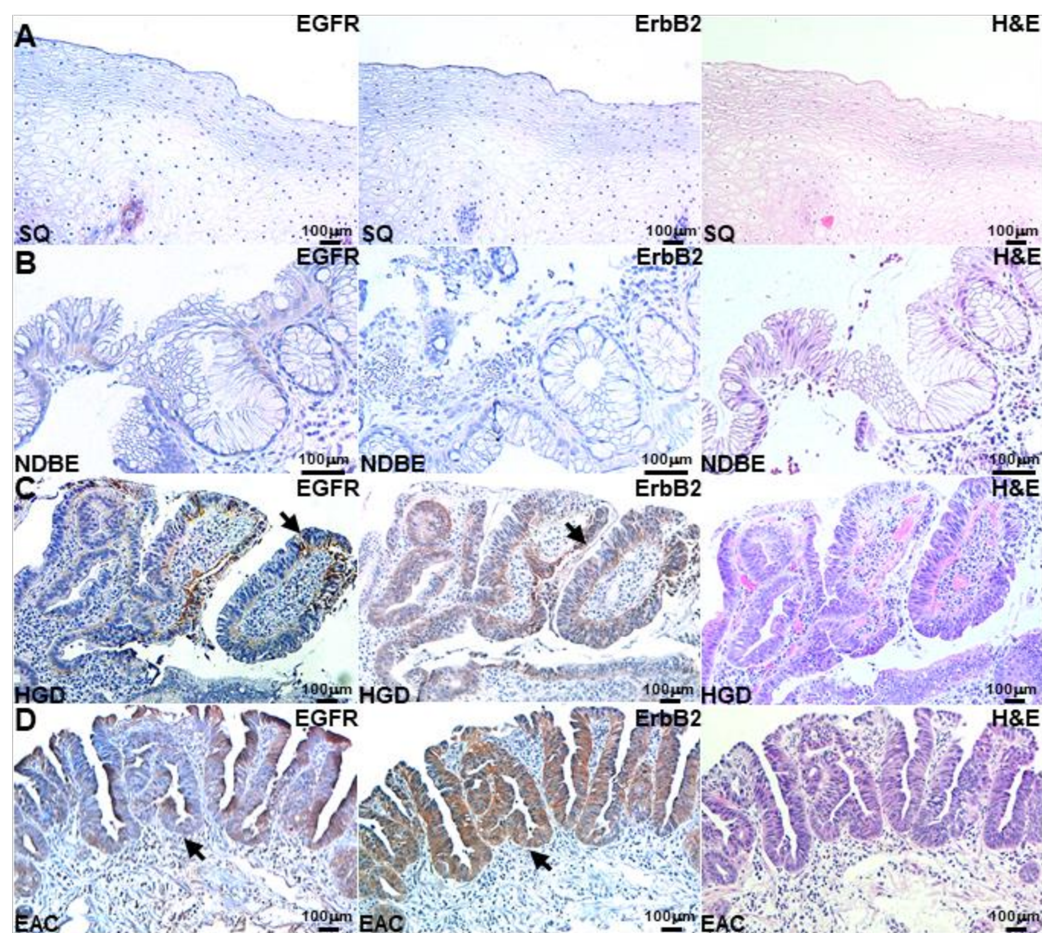


Fig. S1 – Immunohistochemistry. Minimal staining is seen with anti-EGFR and anti-ErbB2 to **A)** SQ and **B)** NDBE, while strong staining is seen to the cell surface (arrow) for **C)** HGD and **D)** EAC. Representative histology (H&E) is shown.

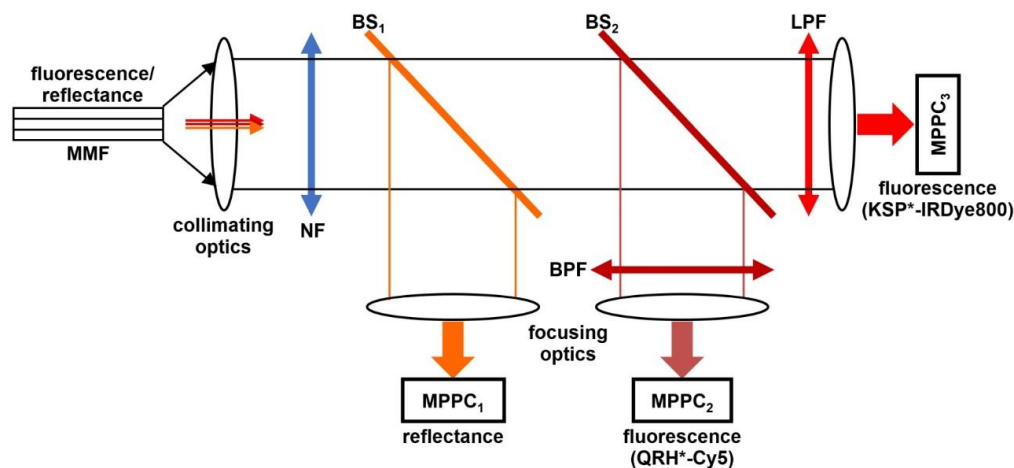


Fig. S2 – Detection scheme. Fluorescence and reflectance are collected and delivered by multi-mode fibers (MMF). A notch filter (NF) attenuates the excitation beam at $\lambda = 785$ nm. Reflectance is deflected by a beam splitter BS₁ with center wavelength at $\lambda = 647$ nm, and detected by a multi-pixel photon counter (MPPC₁). Fluorescence from QRH*-Cy5 is deflected by a dichroic beam splitter (BS₂) centered at $\lambda = 785$ nm. A bandpass filter (BPF) transmits fluorescence between 668-726 nm for detection by MPPC₂. Fluorescence from KSP*-IRDye800 passes through BS₂ and a long pass filter (LPF) with cutoff at $\lambda = 805$ nm for detection by MPPC₃.

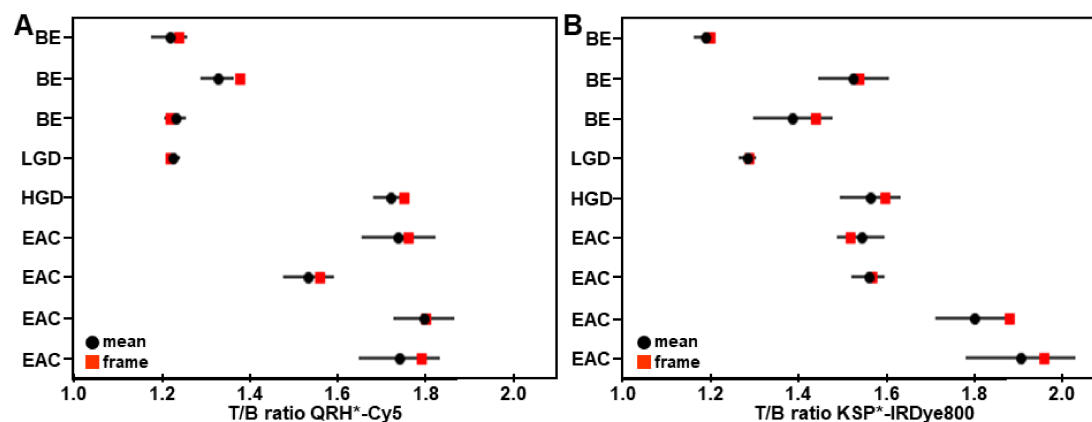


Fig. S3 – T/B variability within video segment. Multiple individual frames were extracted from representative video streams collected in vivo from the esophagus for expression of **A**) EGFR and **B**) ErbB2. The mean (circle) and standard deviation of replicate estimated T/B ratios are shown in black. The square (red) shows the value for the representative frame. For EGFR, the average coefficient of variation (CV), defined as the standard deviation divided by the mean, was 3.2%. The representative images had a 1.2% higher T/B ratio than the average of the replicates, $P = 0.03$ by paired t-test of log-transformed values. Bias was 0.78% higher in the HGD/EAC samples, 1.6% versus 0.8%, $P = 0.45$ by two-sample t-test of the differences of log-transformed data. For ErbB2, the average CV was 4.2%. Representative images had a 1.8% higher T/B ratio than the average of the replicates, $P = 0.015$. Bias was 0.02% lower in the HGD/EAC samples (1.7% versus 1.9%, $P = 0.90$).

Supplementary videos

Video S1 – Peptides are topically administered to the distal esophagus via a standard spray catheter.

Video S2 – After 5 minutes for incubation, unbound peptides are washed away with tap water using an endoscopic irrigator.

Video S3 – The mmSFE is passed through the working channel of the endoscope into the esophageal lumen to collect fluorescence and reflectance images

Video S4 – Real-time white light video of SQ.

Video S5 – Real-time fluorescence video of EGFR expression from SQ.

Video S6 – Real-time fluorescence video of ErbB2 expression from SQ.

Video S7 – Real-time reflectance video from SQ.

Video S8 – Real-time merged video from SQ.

Video S9 – Real-time white light video of NDBE.

Video S10 – Real-time fluorescence video of EGFR expression from NDBE.

Video S11 – Real-time fluorescence video of ErbB2 expression from NDBE.

Video S12 – Real-time reflectance video from NDBE.

Video S13 – Real-time merged video from NDBE.

Video S14 – Real-time white light video of HGD.

Video S15 – Real-time fluorescence video of EGFR expression from HGD.

Video S16 – Real-time fluorescence video of ErbB2 expression from HGD.

Video S17 – Real-time reflectance video from HGD.

Video S18 – Real-time merged video from HGD.

Video S19 – Real-time white light video of EAC.

Video S20 – Real-time fluorescence video of EGFR expression from EAC.

Video S21 – Real-time fluorescence video of ErbB2 expression from EAC.

Video S22 – Real-time reflectance video from EAC.

Video S23 – Real-time merged video from EAC.